FUNCTIONAL
MATERIALS

Fluorescent nanodiamond array deposition on porous anodized aluminum oxide using asperity assisted capillary force assembly

Uldis Malinovskis[a], Andris Berzins[b], Janis Smits[b], Florian H. Gahbauer[b], Ruvin Ferber[b], Donats Erts[a,c], and Juris Prikulis[a]*

[a] Institute of Chemical Physics, University of Latvia, 19 Raina Blvd., Riga LV-1586, Latvia
[b] Laser Centre, University of Latvia, 19 Raina Blvd., Riga LV-1586, Latvia
[c] Faculty of Chemistry, University of Latvia, 19 Raina Blvd., Riga LV-1586, Latvia

Abstract. Array ordering of nanodiamonds with nitrogen-vacancy centers using porous anodized aluminum oxide (PAAO) templates is studied. Particle sorting and array formation are demonstrated with a polydisperse suspension of irregularly shaped diamonds with 28 nm number mean value diameter. The assembly is governed by a balance of withdrawal speed and evaporation driven particle flux, which is influenced by the asperities of the PAAO surface during the capillary and convective assembly dip-coating process. The resulting structures are dense (50 nm average center separation) isolated (non-touching) nanoparticle arrays with a size distribution that matches the topology of the template surface. The fluorescence signal is detected from arrays with an approximately 1:1 particle/pore filling ratio.

Key words: porous anodic alumina, fluorescent nanodiamond, colloid assembly, templated deposition.

1. INTRODUCTION

Nanoparticle arrays are of great interest for designing new devices with increasing component density, e.g. electronic or magnetic memory. One of the emerging multifunctional nanoparticle materials is diamond. As a semiconductor it is expected to be of technological importance for the electronics industry [1]. Fluorescent nanodiamonds (FND) have been proposed for quantum computing and the ability to create ordered arrays of such structures may open new possibilities of complex device design [2]. Other potential FND applications include biomolecular labeling [3], nanophotonic light sources [4], and magnetic imaging [5]. Due to extreme synthesis conditions, the production of FND arrays using lithographic or masked deposition techniques is difficult. However, nanodiamonds can be obtained in colloidal suspensions [6].

In this work we demonstrate porous anodic aluminum oxide (PAAO) templated deposition of commercially available FND, which are manufactured by centrifugation of crushed synthetic monocrystalline diamond powder. As such, the particle shape is highly irregular and not suitable for direct ordered colloidal crystal self-assembly [7,8].

PAAO has been used for the production of nano-structure arrays, either by using electrochemical deposition [9,10], the supercritical fluid method [11], masked deposition [12], imprinting [13], or other methods [14]. However, reports on colloid deposition on PAAO are scarce, although the method is fairly simple and extends the range of possible materials for nanoparticle array synthesis. PAAO has been used as a host for one-dimensional chains of colloidal gold nanoparticles and clusters [15], two-dimensional Au nanoparticle arrays [16], and magnetic nanoparticles [17]. In this work we achieve array ordering by matching the nanoparticle size to pore geometry, ideally approaching the one particle per pore limit.

The key difference from capillary force assisted colloid assembly procedures [7,8,17–19] is the ability to obtain dense non-touching arrays from initially polydisperse suspensions of irregularly shaped particles. Another advantage is that template surfaces are produced by a self-organizing electrochemical process, which is much faster and more cost-effective in comparison to lithographically prepared substrates [20,21]. The method presented here can potentially be scaled for a large variety of available PAAO types with different pore geometries and sample sizes.

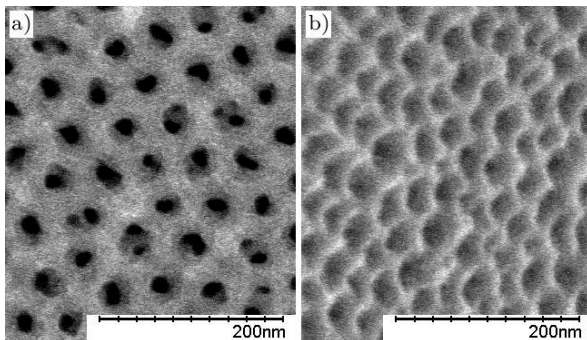* Corresponding author, juris.prikulis@lu.lv

2. EXPERIMENTAL

Type 1B (high-pressure high-temperature synthesis) nitrogen-vacancy (NV) center FND particle solution in water (DiaScence 25, Quantum Particles) with a size $d_{50} = 28$ nm (number mean value), standard deviation 9 nm, concentration 0.29 mg/mL, zeta potential –21 mV was used as received.

The PAAO membranes were produced on bulk 0.25 mm thick high purity (99.999% GoodFellow) electropolished aluminum sheet using a two-stage anodization protocol [12] in 0.3 M sulfuric acid solution at constant voltage 20 V as described elsewhere [22]. The resulting membrane thickness was 150–200 nm, pore opening diameters ≈ 25 nm, and average center separation 50 nm (Fig. 1a).
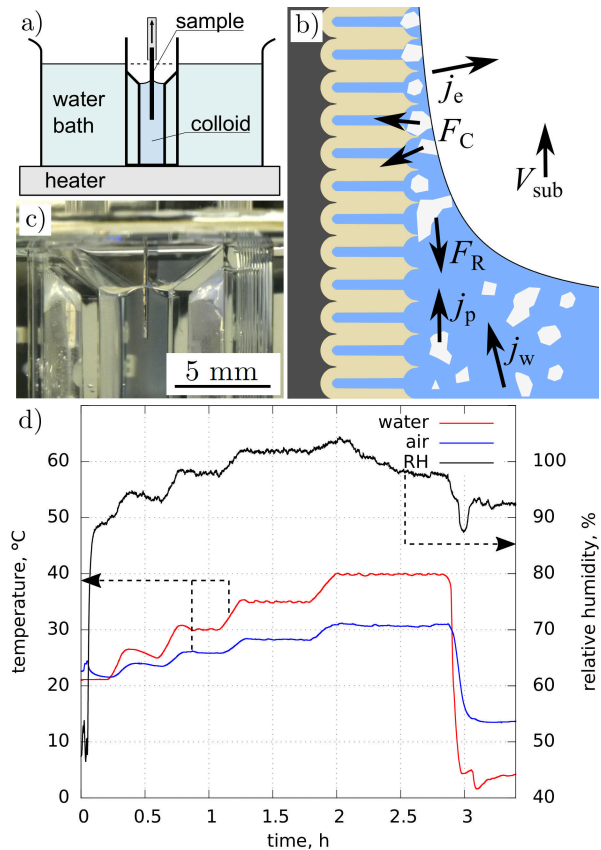
The PAAO coated Al sheet (9×18 mm²) was immersed in the colloid (Fig. 2a, c) and pulled out at constant velocity V_{sub} that could be tuned in 0.1–20 μm/s range using a stepper motor driven translation stage. The meniscus contact angle to substrate is small (below 45°, Fig. 2c), which confirms the hydrophilic nature of the PAAO coating. Finally, the samples were left to dry overnight in air at room temperature. Particle size and distribution analysis was done using a field emission scanning electron microscope (SEM Hitachi S4800).

A relative humidity sensor (HIH-4010-001, Honeywell) and a digital thermometer were mounted on an Al sheet inside the cuvette ≈ 5 mm above the colloid solution and the values were recorded without sample movement (Fig. 2c). A second digital thermometer was used to monitor the water bath temperature and control the thermostat heater against a predefined setpoint, typically 25–40 °C.

For the excitation of the NV centers in nanodiamonds we used a 520 nm diode laser (Osram PLP520). The laser power at the sample was ≈ 60 mW. The laser light was focused on the sample using a microscope lens (40x, NA 0.60, Leica HCX PL Floutar). The fluorescence signal was collected using the same lens and after passing through a series of optical filters (band filter, Edmund Optics 700 ± 40 nm, and two long-pass filters, Melles
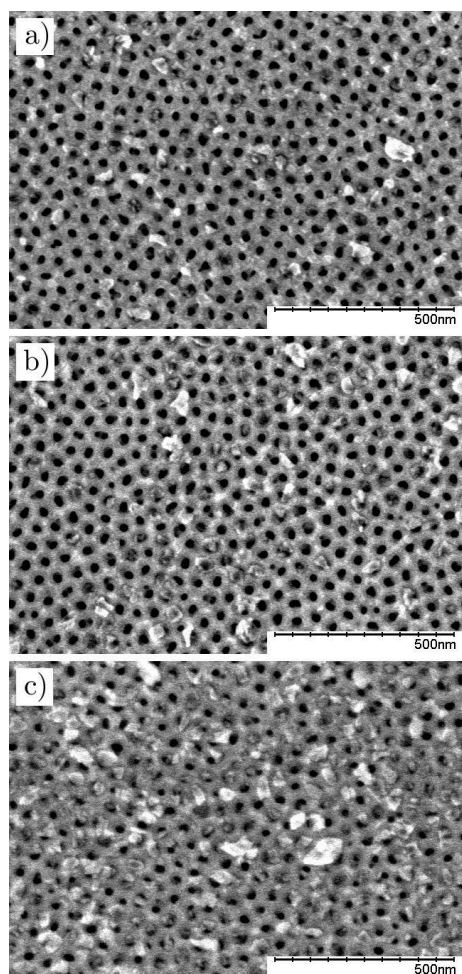
Fig. 2. (a) Schematic of dip-coating set-up, (b) principle of colloid fractioning and ordering process, (c) photograph of the meniscus area during sample withdrawal, (d) relative humidity and temperature measurement inside the cuvette at different water bath temperatures.

Griot 03FCG501, cut-off 600 nm and 03FCG498, cut-off 575 nm), was coupled into an optical fiber with the core diameter of 105 μm that led to a photon multiplier (Hamamatsu H7421-40). The optical set-up was stationary and the sample was scanned using a 3-axis positioning stage (Thorlabs MAX341/M) using 10 μm steps.

3. RESULTS AND DISCUSSION

The temperature dependence of nanodiamond distribution at a fixed withdrawal velocity 2 μm/s is shown in Fig. 3. Nearly all nanodiamonds are located on the funnel shaped pore openings (pore morphology can be seen in Fig. 1b) and the number of filled pores increases with increasing temperatures. Notably, at higher temperatures, more pores tend to host multiple particles. The SEM analysis of pores, which are more than 100 nm deep, does not allow an accurate distinguishing of individual particles from small aggregates. However, even at 40 °C no large aggregates of connected particles or continuous nanoparticle layers are formed.

Fig. 1. SEM image of typical PAAO template as obtained using sulfuric acid electrolyte: (a) top view, (b) tilted view.

Fig. 3. Nanodiamonds on the PAAO surface drawn at constant velocity 2 μm/s and different temperatures: (a) ice bath, (b) 25 °C, (c) 40 °C.

For the demonstration of the surface morphology role in array formation, a series of samples was produced at the same withdrawal velocity and set of temperatures on a flat electropolished aluminum substrate instead of PAAO (Fig. 4). A pure aluminum surface is naturally covered by a thin passivation layer of aluminum oxide and can be considered chemically identical to PAAO, although the latter may contain traces of electrolyte ions. One can immediately observe the nanoparticle fractioning effect on the PAAO substrate since the size of the majority of nanodiamonds is less than the specified number mean $d_{50} = 28$ nm of the colloid. In comparison, on a flat electropolished aluminum surface at 40 °C large areas (tenths of micrometers across) of continuous nanoparticle film are formed (Fig. 4c, f), and at 25 °C the entire sample surface is randomly and uniformly covered with nanoparticles without notable size preference (Fig. 4b, e). However, after the deposition at ice bath temperature, small groups of sparse (not connected) diamond formations can

be observed (Fig. 4a, d). This temperature dependent behavior is similar to convective colloid crystal growth and disassembly at elevated and reduced temperatures as demonstrated using monodisperse solutions [8]. One can also notice that surface features, such as aluminum grain boundaries (narrow lines in Fig. 4f) or variations of topology due to different etching rates depending on crystallographic orientation, influence the formation of nanodiamond arrays.

The next observation is that on a flat aluminum surface the smaller nanodiamonds (size below approx. 20 nm) are well separated by a characteristic distance of about 30–40 nm, whereas larger ones tend to aggregate. The aggregation increases at higher temperatures reaching full coverage at 40 °C and withdrawal speed 2 μm/s (Fig. 4c). In contrast, large aggregates are nearly absent if deposition is done under identical conditions on the PAAO surface (Fig. 3c).

The colloid deposition on the PAAO surface in the dip-coating process involves multiple mechanisms and competing forces, such as particle–particle and particle–substrate interactions, convection, and water–air surface tension, which is beyond the scope of this article (see detailed description in [23]). In brief, the evaporation flux j_e from the thin liquid layer above the meniscus is compensated by water flux j_w, which also drives particles towards the evaporation region (Fig. 2b). The particle flux is hindered by interactions with the surface, which are stronger for a porous alumina in comparison to a flat alumina surface. The balance between withdrawal velocity V_{sub} and particle flux j_p due to evaporation is the dominant factor, which determines the array density. The characteristic distance (30–40 nm) between the smaller nanodiamonds (size below the number mean) on a flat aluminum surface as determined by the double layer interaction is similar or slightly less than the pore separation in PAAO, which is a favorable factor for complete pore filling with smaller particles. Additionally the asperities reduce the contact area (or effective radius) between the diamond and aluminum oxide surfaces for particles with size exceeding the pore opening funnel diameter. This in turn reduces the adhesion forces between particles and the substrate causing the meniscus capillary forces to effectively remove the largest diamond crystals from the PAAO membrane with a net force F_R. The actual pore filling and array ordering (particle centering force F_C) occurs while drying the sample surface after the thickness of the water layer has been reduced below the asperity height. The particles are captured between asperities and directed to pore cavity by capillary forces of the remaining liquid.

The relative air humidity (RH) in the lab was kept at approximately 50%. At ice bath temperatures, the RH inside the cuvette is over 90%. At increased colloid temperatures, the humidity increases, saturates at 30 °C, and at 40 °C water starts to condense at cuvette walls above the liquid surface and RH drops slightly below 100%. However, there is little correlation between the observed array density and the measured RH value. The important parameter is the required vapor flux to maintain the
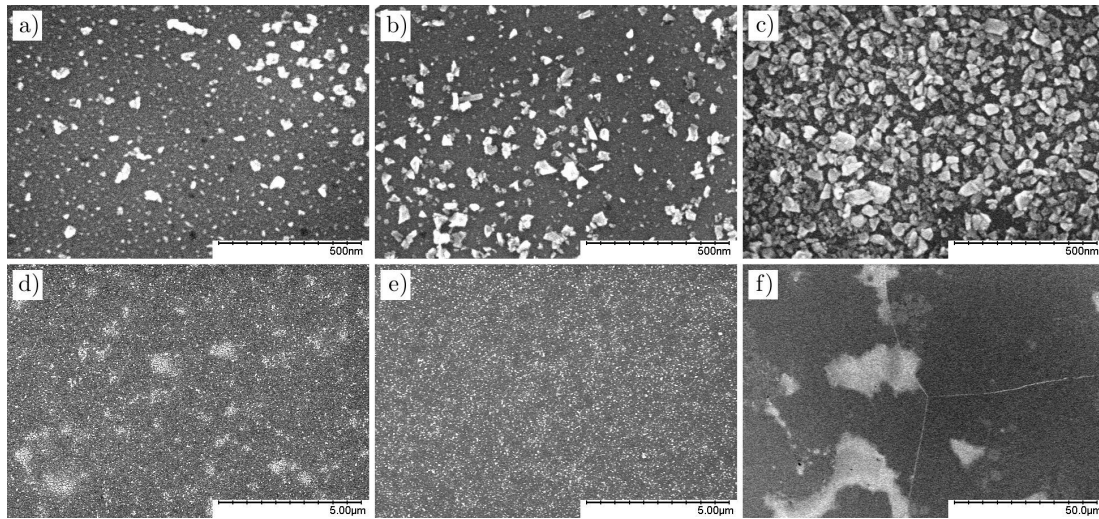
Fig. 4. Nanodiamonds on the electropolished aluminum surface drawn at constant velocity 2 μm/s and different temperatures: (a) ice bath, (b) 25 °C, (c) 40 °C; (d,e,f) low magnification images of (a,b,c).

dynamic equilibrium of the RH near the liquid surface. This depends on the temperature differences between the colloid, aluminum sample, and cuvette walls and derives from the heating or cooling regime. At 40 °C, the immersed aluminum sample is significantly warmer than the surrounding air, which causes a high evaporation rate of the thin liquid layer above the meniscus. This in turn increases the nanoparticle flux and the formation of dense layers as can be seen in Fig. 4c, f. In the opposite case (ice-bath), the aluminum sample is colder than the surrounding air and causes condensation of water on its surface. This may reverse the water flux and separate the particles that have been trapped by the meniscus and the viscous drag [8].

Now we turn our attention to the role of withdrawal velocity. The particle density increases at lower pullout rates (Fig. 5). Although it is difficult to measure the density quantitatively, the obtained density ratios are similar to those achieved by varying the temperature (Fig. 3). Namely, the increase of the withdrawal speed is equivalent to the reduction of the colloid temperature.

Either of the control parameters, colloid temperature or withdrawal velocity, can be used to tune the nanodiamond array density. Since the velocity can be changed instantaneously, it is a convenient way to produce multiple regions with predefined densities on the same sample for further experiments. A particular question one may ask is whether the photoluminescence from the aluminum oxide, which peaks typically at 460 nm [24], is sufficiently small for NV fluorescence detection at wavelengths above 600 nm. The type of nanodiamonds used in the present study was reported to have on average 1–2 NV centers per particle [25]. For this purpose 1 mm wide zones of different density (Fig. 6a) were produced by cyclic switching of V_{sub} between 0.4, 2, and 11 μm/s. Despite the
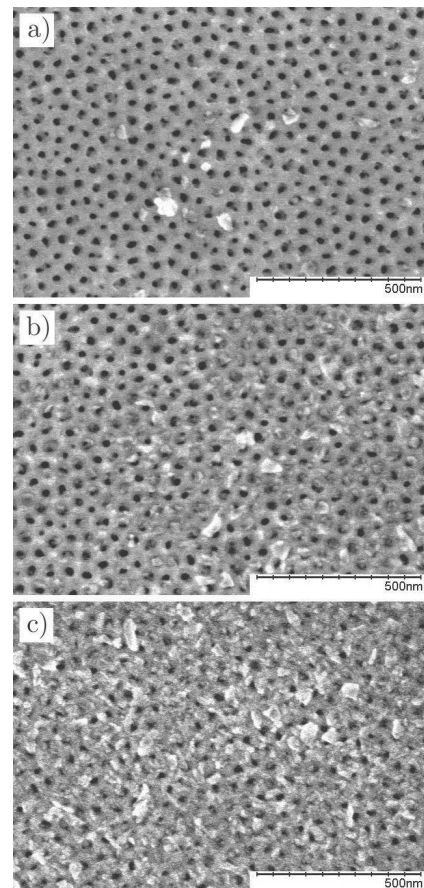
Fig. 5. Nanodiamonds on the PAAO surface drawn at constant temperature 40 °C and different velocities: (a) 11 μm/s, (b) 2 μm/s, (c) 0.4 μm/s.
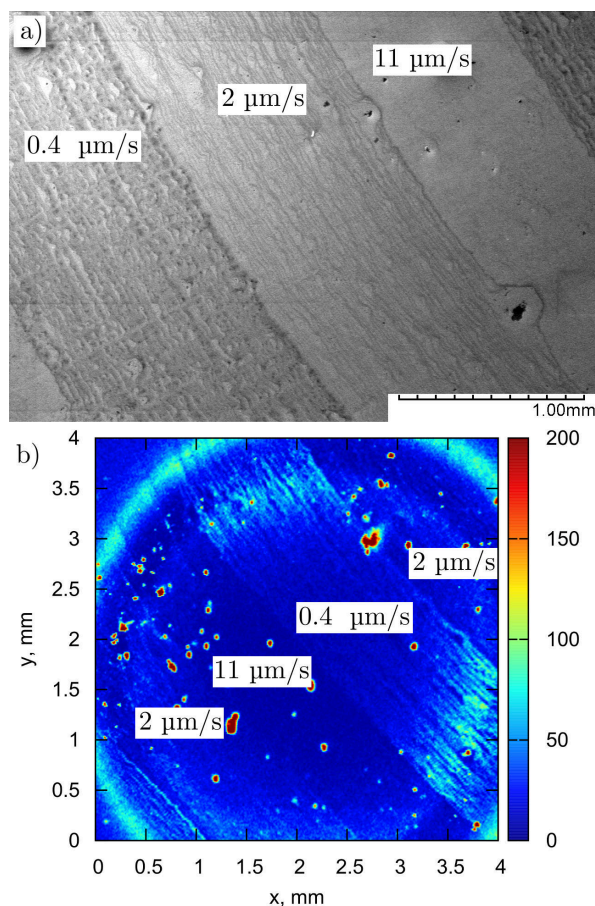
Fig. 6. (a) Low magnification SEM image of nanodiamond arrays obtained on a single PAAO substrate by setting different withdrawal velocities. (b) Fluorescence image of the same sample. The pseudo-color scale shows photon multiplier counts at each pixel.

concentric artefacts, which are most likely caused by stray light during sample scanning, all three zones can be clearly identified in the fluorescence image (Fig. 6b). This shows that fluorescence from nanodiamonds at an approximately $1 : 1$ pore filling ratio ($2\ \mu$m/s case, Fig. 5b) can be distinguished from possible photoluminescence background from the alumina template. Hence individual nanodiamonds on PAAO could be potentially detected using higher resolution techniques such as confocal, nearfield, or stochastic reconstruction microscopy methods.

4. CONCLUSIONS

We have studied the applicability of PAAO membranes for the production of ordered nanoparticle arrays. In addition to traditional templated deposition techniques, PAAO provides size-dependent fractioning of polydisperse colloids. The PAAO membrane obtained using 0.3 M sulfuric acid electrolyte at 20 V potential is a very

suitable template material for ordering FND, since the pore morphology closely matches nanocrystal size and host and guest photoluminescence do not overlap.

Considering the polydispersity and shape irregularity of the initial nanodiamond suspension (Fig. 4), the resulting arrays are highly uniform and well ordered (short range ordering) in a formation determined by the PAAO membrane structure. Clearly the array quality could be improved when monodisperse and round nanoparticles are available [23]; however, for FND this remains a challenging goal.

REFERENCES

1. Wort, C. J. H. and Balmer, R. S. Diamond as an electronic material. *Mater. Today*, 2008, **11**, 22–28.
2. Albrecht, A., Koplovitz, G., Retzker, A., Jelezko, F., Yochelis, S., Porath, D., et al. Self-assembling hybrid diamond-biological quantum devices. *New J. Phys.*, 2014, **16**(9), 093002.
3. Yu, S. J., Kang, M. W., Chang, H. C., Chen, K. M., and Yu, Y. C. Bright fluorescent nanodiamonds: no photobleaching and low cytotoxicity. *J. Am. Chem. Soc.*, 2005, **127**(50), 17604–17605.
4. Schietinger, S., Barth, M., Aichele, T., and Benson, O. Plasmon-enhanced single photon emission from a nanoassembled metal-diamond hybrid structure at room temperature. *Nano Lett.*, 2009, **9**(4), 1694–1698.
5. Smits, J., Berzins, A., Gahbauer, F. H., Ferber, R., Erglis, K., Cebers, A., et al. Estimating the magnetic moment of microscopic magnetic sources from their magnetic field distribution in a layer of nitrogen-vacancy (NV) centres in diamond. *Eur. Phys. J. Appl. Phys.*, 2016, **73**(2), 20701.
6. Mochalin, V. N, Shenderova, O., Ho, D., and Gogotsi, Y. The properties and applications of nanodiamonds. *Nat. Nanotechnol.*, 2011, **7**(1), 11–23.
7. Dimitrov, A. S. and Nagayama, K. Continuous convective assembling of fine particles into two-dimensional arrays on solid surfaces. *Langmuir*, 1996, **12**(5), 1303–1311.
8. Malaquin, L., Kraus, T., Schmid, H., Delamarche, E., and Wolf, H. Controlled particle placement through convective and capillary assembly. *Langmuir*, 2007, **23**(23), 11513–11521.
9. Huang, C. H., Lin, H. Y., Tzeng, Y., Fan, C. H., Liu, C. Y., Li, C. Y., et al. Optical characteristics of pore size on porous anodic aluminium oxide films with embedded

silver nanoparticles. *Sens. Actuators A Phys.*, 2012, **180**, 49–54.

10. Baitimirova, M., Pastare, A., Katkevics, J., Viksna, A., Prikulis, J., and Erts, D. Gold nanowire synthesis by semi-immersed nanoporous anodic aluminium oxide templates in potassium dicyanoaurate-hexacyanoferrate electrolyte. *Micro Nano Lett.*, 2014, **9**(11), 761–765.

11. Polyakov, B., Prikulis, J., Grigorjeva, L., Millers, D., Daly, B., Holmes, J. D., et al. Photoconductivity of germanium nanowire arrays incorporated in anodic aluminum oxide. *J. Phys. Conf. Ser.*, 2007, **61**(1), 283–287.

12. Masuda, H. and Satoh, M. Fabrication of gold nanodot array using anodic porous alumina as an evaporation mask. *Jpn. J. Appl. Phys.*, 1996, **35** (Part 2, No. 1B), L126–L129.

13. Zhan, Z. and Lei, Y. Sub-100-nm nanoparticle arrays with perfect ordering and tunable and uniform dimensions fabricated by combining nanoimprinting with ultrathin alumina membrane technique. *ACS Nano*, 2014, **8**(4), 3862–3868.

14. Lee, W. and Park, S. J. Porous anodic aluminum oxide: anodization and templated synthesis of functional nanostructures. *Chem. Rev.*, 2014, **114**(15), 7487–7556.

15. Hornyak, G., Kröll, M., Pugin, R., Sawitowski, T., Schmid, G., Bovin, J. O., et al. Gold clusters and colloids in alumina nanotubes. *Chem. Eur. J.*, 1997, **3**(12), 1951–1956.

16. Hsu, C. and Liu, H. H. Optical behaviours of two dimensional Au nanoparticle arrays within porous anodic alumina. *J. Phys. Conf. Ser.*, 2007, **61**, 440–444.

17. Seo, I., Kwon, C. W., Lee, H. H., Kim, Y. S., Kim, K. B., and Yoon, T. S. Completely filling anodic aluminum oxide with maghemite nanoparticles by dip coating and their magnetic properties. *Electrochem. Solid State Lett.*, 2009, **12**(9), K59.

18. Park, H., Kim, T. H., Kang, S. W., and Jeong, S. H. Nanoscale reaction vessels: highly ordered nanocrystal arrays inside porous anodic alumina nanowells. *Int. J. Electrochem. Sci.*, 2015, **10**, 8447–8453.

19. Gordon, M. J. and Peyrade, D. Separation of colloidal nanoparticles using capillary immersion forces. *Appl. Phys. Lett.*, 2006, **89**(5), 053112.

20. Kuemin, C., Cathrein Huckstadt, K., Lörtscher, E., Rey, A., Decker, A., Spencer, N. D., and Wolf, H. Selective assembly of sub-micrometer polymer particles. *Adv. Mater.*, 2010, **22**(25), 2804–2808.

21. Virganavičius, D., Juodėnas, M., Tamulevičius, T., Schift, H., and Tamulevičius, S. Investigation of transient dynamics of capillary assisted particle assembly yield. *Appl. Surf. Sci.*, 2017, **406**, 136–143.

22. Malinovskis, U., Poplausks, R., Apsite, I., Meija, R., Prikulis, J., Lombardi, F., et al. Ultrathin anodic aluminum oxide membranes for production of dense sub-20 nm nanoparticle arrays. *J. Phys. Chem. C.*, 2014, **118**(16), 8685–8690.

23. Malinovskis, U., Berzins, A., Gahbauer, F. H., Ferber, R., Kitenbergs, G., Muiznieks, I., et al. Colloidal nano-particle sorting and ordering on anodic alumina patterned surfaces using templated capillary force assembly. *Surf. Coat. Technol.*, 2017, **326**, 264–269.

24. Li, G. H., Zhang, Y., Wu, Y. C., and Zhang, L. D. Wavelength dependent photoluminescence of anodic alumina membranes. *J. Phys. Cond. Matter*, 2003, **15**(49), 8663–8671.

25. Chang, K., Eichler, A., Rhensius, J., Lorenzelli, L., and Degen, C. L. Nanoscale imaging of current density with a single-spin magnetometer. *Nano Lett.*, 2017, **17**(4), 2367–2373.

Fluorestseeruva nanoteemandi ridade sadestamine poorsele anoodalumiiniumoksiidile, kasutades ebatasasusest tingitud kapillaarjõude

Uldis Malinovskis, Andris Berzins, Janis Smits, Florian H. Gahbauer, Ruvin Ferber, Donats Erts ja Juris Prikulis

On uuritud nanoteemandi ridade moodustumist poorsetel anoodalumiiniumoksiidist trafarettidel. Osakeste korrastamist sellistel alustel jälgiti dispersses suspensioonis, mis sisaldas ebaregulaarse kujuga teemandiosakesi keskmise läbimõõduga 28 nm. On näidatud, et sukelduskatmise protsessis juhib osakeste korrastumist tasakaal aluse lahusest väljatõmbamise ja lahuse aurustumise kiiruse vahel. See tasakaal sõltub omakorda pinna ebatasasusest ja sellest mõjutatud kapillaarjõududest ning konvektsioonist lahuses. Töö tulemusena saadi fluorestseeruvad struktuurid, kus üksteisest eraldatud nanoosakesed paiknevad tihedalt pakitud (sammuga 50 nm) ridadena.